Disorder effects in LaAlO$_3$:Ho^{3+} single crystals revealed by optical spectra

K. N. Boldyrev [1,*] N. M. Abishev [2] I. E. Mumdzi,[2] S. I. Nikitin [2] P. J. Deren [3] B. Z. Malkin [2] and M. N. Popova [1]

[1]*Institute of Spectroscopy RAS, Troitsk, Moscow 108840, Russia*
[2]*Kazan Federal University, Kazan 420008, Russia*
[3]*Institute of Low Temperatures and Structure Researches, Polish Academy of Sciences, P. O. Box 1410, 50-950 Wroclaw 2, Poland*

High-resolution spectroscopic studies of LaAlO$_3$ single crystal doped with holmium ions are reported. Polarized and unpolarized absorption and luminescence spectra were measured in the broad spectral range from 2000 to 23 000 cm^{-1} at temperatures of 4.5–5 K. Additional measurements were fulfilled using site-selective laser spectroscopy. Energies and symmetry properties of the corresponding wave functions of crystal-field levels of Ho^{3+} ions which substitute for La^{3+} ions in LaAlO$_3$ at sites with the D_3 symmetry were determined with high accuracy, and, on this basis, crystal-field calculations were performed. A thorough analysis of spectral line profiles with the fine doublet structure corresponding to singlet-doublet transitions in the trigonal crystal field was made, which showed the existence of the random deformation splitting phenomenon. The value of deformation splitting lies in the region 0.3–0.8 cm^{-1} that substantially exceeds the widths of the doublet hyperfine splitting. The observed line shapes were successfully modeled, assuming the interaction of the Ho^{3+} ions with random deformations of the crystal lattice induced by point defects and ferroelastic domain boundaries.

I. INTRODUCTION

Crystals with a general formula ABX_3 and a perovskite structure have many attractive properties that make them interesting for both solid state physics and applications. Classical perovskite is the CaTiO$_3$ mineral; it was discovered in 1839 by Gustav Rose in the Ural Mountains and named after the amateur mineralogist and minister of this region in the Russian Empire, Lev Perovski. Depending on the elements in the structure, synthetic perovskites show ferroelectricity [1], piezoelectricity [2], pronounced multiferroic properties [3], giant magnetoresistance [4], and superconductivity [5]. Hybrid organic-inorganic perovskites opened a new era for low-cost, high-efficiency solar cells [6,7]; they also have a potential for light emitting diodes [8], lasers [9], photodetectors [10], and thermoelectric devices [11]. There are various perovskite phosphors with attractive luminescent properties (see, e.g., Ref. [12], and references therein).

Among other perovskites, lanthanum aluminate LaAlO$_3$ (LAO) stands out for such properties as high dielectric constant [13], broad optical band gap ($\sim$5.5 eV [14]), good thermal stability, and high immunity against environmental moisture; it finds many applications in various fields of technology. In particular, LAO is used as substrates for epitaxial crystal growth, synthesis of thin-film heterostructures and high-temperature superconducting layers, as gate dielectrics in various transistors [15,16], and as a catalyst [17,18]. The discovery of a high-mobility electron gas at the LaAlO$_3$/SrTiO$_3$ heterointerface [19] has stimulated a lot of research aimed at using these interfaces in modern technologies. Recently, over 100-THz bandwidth selective difference frequency generation was reported at LaAlO$_3$/SrTiO$_3$ nanojunctions [20]. Rare-earth (RE) doped LAO crystals can be used as luminophors [12,21–28] and laser hosts [29].

In the high-temperature phase, the lanthanum aluminate has a cubic symmetry with the space group $Pm\bar{3}m$. The spontaneous lattice deformation that mainly involves rotations of AlO$_6$ octahedra around one of the C_3 symmetry axes induces the structural transition into the rhombohedral phase $R\bar{3}c$ at the temperature $T_S = 813$ K [30]. In the $R\bar{3}c$ phase, the unit cell contains six formula units, La^{3+} ions are at the $6a$ sites with the coordinates $(0, 0, 1/4)$, Al^{3+} ions at the $6b$ sites $(0, 0, 0)$, and O^{2-} ions at the $18e$ sites $(x, 0, 1/4)$. There are 12 O^{2-} ions in the nearest surroundings of La^{3+} ions at distances from 2.516 to 2.814 Å [31].

Upon cooling the LAO crystals below T_S, a ferroelastic twin-domain structure is formed [32]. Twin boundaries are a source of internal strains in microscopically inhomogeneous samples and can strongly affect the spectral properties of impurity centers in LAO.

Optical spectra of LAO crystals doped with RE ions Pr^{3+} [21,33], Nd^{3+} [29], Eu^{3+} [22], Ho^{3+} [23], Er^{3+} [24], and Tm^{3+} [25], which substitute for La^{3+} ions at sites with the local D_3 symmetry, demonstrate strong inhomogeneous broadening and contain a large number of spectral lines corresponding to the f-f transitions. The broadening can be caused by random fields of different nature affecting the $4f$ electrons, in particular, by random strains in the crystal lattice. It should be noted that in the case of orbital degeneracy of the crystal-field (CF) energy levels, random elastic deformations can induce formation of the fine structure in the optical spectra of RE ions. The deformation splittings of optical spectral lines was observed earlier in the high-resolution optical spectra of RE-doped crystals with the scheelite [34,35], elpasolite [36], and zircon [37] structures. In [34–37], the observed specific

*kn.boldyrev@gmail.com

profiles of spectral lines were successfully interpreted within the framework of the deformation broadening and splitting model, in which point defects act as a source of random lattice distortions.

Absorption and emission spectra of LAO doped with Ho^{3+} ions were measured at temperatures of 10–300 K and analyzed in Ref. [23]. A number of the obtained CF sublevels of some multiplets of Ho^{3+} exceeded the corresponding number of sublevels allowed by the D_3 symmetry, and the CF analysis was not performed.

In the present work, high-resolution optical absorption and luminescence spectra of LAO single crystal doped with the Ho^{3+} ions were measured in a wide range of wavelengths. For more accurate identification of spectral lines and determination of CF energies, the methods of site-selective laser spectroscopy were also used. The analysis of the registered spectra in the framework of the CF approximation allowed us to determine CF parameters and successfully describe the constructed energy patterns of the Ho^{3+} multiplets.

Some of the measured spectral lines of Ho^{3+} have specific inhomogeneously broadened profiles with shallow dips at the line center. We assume that the observed line shapes are caused by the interaction of $4f$ electrons with local deformations induced by point lattice defects and with internal lattice distortions caused by the sample microstructure. Due to markedly different ionic radii of La^{3+} (1.032 Å) and Ho^{3+} (0.9 Å) [38], the substitution of Ho^{3+} for La^{3+} is accompanied by displacements of lattice ions from their equilibrium positions in the nearest surrounding of the impurity Ho^{3+} ions. Thus, the impurity RE ions themselves as well as the intrinsic lattice defects, in particular, oxygen vacancies [39,40], can be considered as point defects in activated LAO crystals. To account for the influence of these point defects on the line shapes, we use the previously developed theory of the deformation broadening and splitting of spectral lines of optical centers due to point defects in an elastically anisotropic continuum [36]. The peculiarity of LAO crystals is the existence of the twin domains below the temperature ~800 K

of the cubic-rhombohedral phase transition. The twin-domain boundaries serve as an additional source of random lattice deformations. Here, we develop an approach to take into account this source of deformations when modeling the observed line shapes. We estimate the width of the distribution of local deformations in the studied sample of LAO:Ho^{3+} using the obtained spectroscopic data.

II. EXPERIMENT

A $LaAlO_3$ crystal was grown by the Czochralski method at Union Carbide, USA. The concentration of Ho^{3+} was 0.5 wt %. A sample in the shape of a parallelepiped with dimensions 5.0 mm × 4.0 mm × 2.2 mm was cut and polished.

Optical absorption and luminescence spectra in the spectral range 2000–22 000 cm^{-1} at the temperatures of 4.5–5 K were measured using a high-resolution Fourier spectrometer, Bruker IFS 125 HR, equipped with Si and InSb detectors. The spectral resolution for the absorption measurements was up to 0.01 cm^{-1}. To excite the photoluminescence (PL), the emission of the cw multimode red diode laser (wavelength 635 nm, power 50 mW) was focused on the sample in a spot of about 0.5 mm in diameter. For low-temperature experiments, we used a closed-cycle helium cryostat, Cryomech PT403.

A pulsed tunable dye laser (Littrow type oscillator and amplifier, linewidth of about 0.5 Å) pumped by the third harmonic of a Nd-YAG laser (LQ129, Solar LS) was used for site-selective spectroscopy. The spectra were analyzed with a MDR-23 monochromator. Spectral resolution was about 1 Å. The luminescence signal was detected by a cooled photomultiplier (PMT-106 or PMT-83) in the photon-counting mode. The studied $LaAlO_3$:Ho^{3+} crystal was kept in helium vapor at a temperature of 4.2 K.

III. EXPERIMENTAL RESULTS

A. Crystal-field levels of Ho^{3+} (D_3-symmetry sites) in $LaAlO_3$

Low-temperature unpolarized transmission and luminescence spectra of LAO :Ho^{3+} in the whole studied spectral
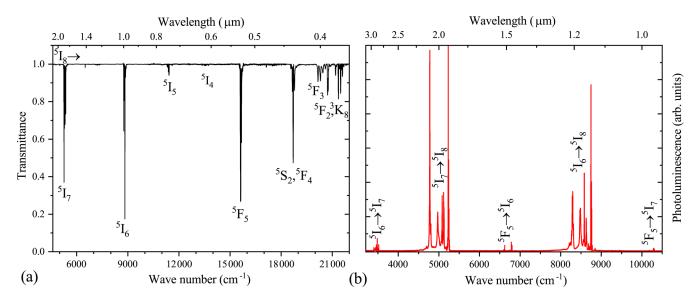

FIG. 1. Unpolarized (a) transmission and (b) luminescence spectra of the LAO:Ho (0.5 wt %) single crystal at 5 K. The crystal thickness in (a) was 2.2 mm. In (b), the excitatation wavelength was 635 nm.

TABLE I. Allowed ED and MD transitions for ions with even number of electrons in the case of D_3 site symmetry. d_i and $\mu_i (i = x, y, z)$, are components of the ED and MD moments, respectively; z axis is parallel to the C_3 symmetry axis.

D_3	Γ_1	Γ_2	Γ_3
Γ_1	$-$	$d_z \mu_z$	$d_x, d_y \mu_x, \mu_y$
Γ_2	$d_z \mu_z$	$-$	$d_x, d_y \mu_x, \mu_y$
Γ_3	$d_x, d_y \mu_x, \mu_y$	$d_x, d_y \mu_x, \mu_y$	$d_x, d_y, d_z \mu_x, \mu_y, \mu_z$

range are shown in Fig. 1. Numerous narrow absorption lines correspond to the optical transitions from the ground state to excited multiplets, indicated in Fig. 1(a). Lines in the luminescence spectra are due to transitions from the lowest CF levels of the excited multiplets to the lower-lying CF levels.

Multiplets of the Ho^{3+} ion in the crystal field of the D_3 symmetry split into singlets Γ_1 and Γ_2 and doublets Γ_3 [here Γ_i is the irreducible representation (IR) of the point symmetry group D_3]. Selection rules for electric-dipole (ED) and magnetic-dipole (MD) optical transitions between CF levels are summarized in Table I.

LAO has a pseudocubic structure with four types of twin domains associated with four [111]-type equivalent C_3 axes of the parent cubic phase [32]. Domain boundaries can be seen by the naked eye. Figure 2 shows a microphotograph of our sample with clearly visible domains. If there were an equal number of different domains, no polarization dependence would be observed in optical spectra. In our experiments, with a diaphragm 1 mm in diameter, we selected a region of the sample in which only one direction of the domain walls was visible. The measured absorption spectra strongly depended on the polarization of the incident light. Figure 3 presents examples of the polarized spectra of several multiplets. Some lines are observed in only one polarization and completely disappear in the perpendicular, which confirms that we are dealing with one type of domain.

At 5 K, only the ground state of Ho^{3+} is populated (the gap between the ground state and the first excited CF sublevel equals 26 K; see below). However, the number of observed spectral lines exceeds the maximum number of the CF levels
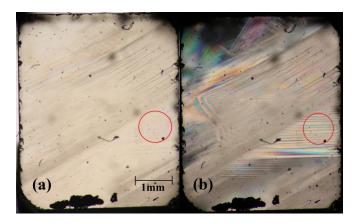

FIG. 2. Microphotograph of the LAO:Ho sample (a) in the unpolarized light and (b) between crossed polarizers. Red circle shows the area for polarized spectroscopic measurements.

allowed by the D_3 symmetry, as has already been noted in Ref. [23]. Evidently, there are additional holmium sites in the structure. We suppose that the additional spectral lines in the measured spectra correspond to transitions in strongly perturbed Ho^{3+} centers located near the ferroelastic twin-domain walls. Also, local lattice deformations can remove the selection rules for the D_3 symmetry, and some low-intensity spectral lines corresponding to forbidden Γ_1-Γ_1 transitions are observed. The site-selective laser spectroscopy allowed us to identify the spectral lines corresponding to transitions in the Ho^{3+} ions at the sites with the local D_3 symmetry.

Figure 4 compares the low-temperature absorption spectra in the region of the $^5I_8 \rightarrow ^5I_7$ transition with the luminescence and site-selective emission spectra in the region of the $^5S_2 \rightarrow ^5I_7$ transition. The CF levels of the $^5S_2$ and $^5F_4$ multiplets (see Table II) were found from the excitation spectrum of the emission from the lowest $^5S_2$ sublevel registered at the frequency of 18 078 cm^{-1} corresponding to the zero-phonon transition $A(^5S_2) \rightarrow K(^5I_8)$. The emission spectra selectively excited at the frequencies 18 571 cm$^{-1}[A(^5I_8) \rightarrow A(^5S_2)]$ and 18 661 cm$^{-1}[A(^5I_8) \rightarrow B(^5F_4)]$ were used to construct the schemes of CF levels in the $^5I_6$ and $^5I_7$, $^5I_8$ multiplets, respectively.

Table II lists the energies of the CF levels of the holmium ions in LAO. The symmetry properties of wave functions (IR) of the CF sublevels of the ground and excited multiplets were determined using the selection rules for optical transitions in the centers with the local D_3 symmetry. The ground state of the Ho^{3+} ions in LAO is the singlet Γ_1. The set of CF energies determined in the present work differs markedly from the one found in Ref. [23].

B. Deformation splittings of the spectral lines

For several transitions between the singlet and the doublet states of the Ho^{3+} ion, corresponding spectral lines have a specific line shape with a narrow dip at the center of the line. These transitions in absorption are shown schematically in Fig. 5; their energies are listed in Table III, together with the measured half widths and splittings. The insets of Figs. 3(b), 3(c), and 6 illustrate the discussed line profiles. Such line shape is induced by random lattice deformations [34–37]. Similar line profiles of the same inverse transitions were registered in the luminescence spectra, but also additional lines with a fine doublet and triplet structure were observed corresponding to the transitions $\Gamma_1(A\ ^5I_6) \rightarrow \Gamma_3(F\ ^5I_7)$ and $\Gamma_3(B\ ^5I_6) \rightarrow \Gamma_3(C\ ^5I_7)$, respectively.

IV. CALCULATIONS OF THE HYPERFINE STRUCTURE OF SINGLET-DOUBLET TRANSITIONS

The energies of the CF levels of the ground and excited multiplets of the Ho^{3+} ions determined from the measured optical spectra were analyzed by making use of the Hamiltonian operating in the space of 1001 states of the ground electronic $4f^{10}$ configuration. The considered Hamiltonian of the Ho^{3+} ion,

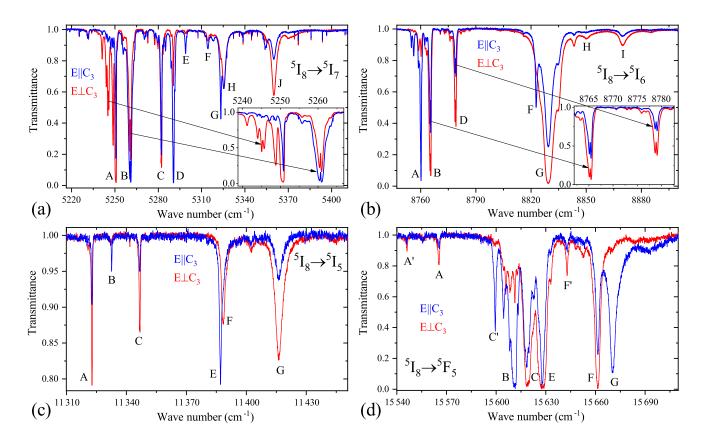$$H_0 = H_{FI} + H_{CF}, \qquad (1)$$

FIG. 3. The transmission spectra of the 2.2 mm thick LAO:Ho (0.5 wt %) single crystal at 5 K in the region of the transitions from the ground state to the (a) $^5I_7$, (b) $^5I_6$, (c) $^5I_5$, and (d) $^5F_5$ multiplets, in the two mutually perpendicular polarizations $\mathbf{E}||C_3$ (blue curves) and $\mathbf{E}\perp C_3$ (red curves). Capital letters denote the final energy levels of the transitions in the corresponding multiplets. The insets show lines with deformation splittings on an enlarged scale. Additional lines corresponding to transitions from the first excited sublevel of the ground multiplet, B (Γ_3), are observed, in particular, lines A', C', and F' shifted to lower frequencies by 18 cm^{-1} from the lines A, C, and F in panel (d).

contains the energies of a free ion (H_{FI}) and of the interaction with the crystal field (H_{CF}). The free-ion Hamiltonian is written in the standard form [41],

$$H_{FI} = \zeta \sum_k \boldsymbol{l}_k \boldsymbol{s}_k + \alpha \hat{\boldsymbol{L}}^2 + \beta \hat{G}(G_2) + \gamma \hat{G}(R_7)$$
$$+ \sum_q (F^q \hat{f}_q + P^q \hat{p}_q + T^q \hat{t}_q + M^q \hat{m}_q), \qquad (2)$$

where $\boldsymbol{l}_k$ and $\boldsymbol{s}_k$ are the operators of the orbital and spin moments of the $4f$ electrons, respectively; $\boldsymbol{L} = \sum_k \boldsymbol{l}_k$ is the operator of the total orbital moment; F^q are the Slater parameters of the electrostatic interactions between $4f$ electrons; ζ is the spin-orbit coupling constant; α, β, γ, and T^q are the parameters of two- and three-particle electrostatic interconfigurational interactions, respectively; the parameters P^q and M^q define the spin-orbit and spin-spin interactions between $4f$ electrons, respectively. The operators $\hat{G}, \hat{f}, \hat{p}, \hat{t}, \hat{m}$ are defined in the literature (see, e.g., [41], and references therein). In our calculations, we started from the free-ion parameters presented in Ref. [42] for the impurity Ho^{3+} ions in YAl$_3$(BO$_3$)$_4$ crystals. Then, these parameters were slightly corrected to fit the centers of gravity of the studied optical multiplets. The final set of the free-ion parameters is presented in Table S1 in the Supplemental Material [43] (also see [44–52]).

The Hamiltonian of the Ho^{3+} ion at the La^{3+} site in the crystal field of the D_3 symmetry, in the Cartesian system of coordinates with the z axis along the C_3 symmetry axis and the x axis along the local C_2 symmetry axis in the crystallographic ab plane, is defined by six real CF parameters B_p^k and has the following form:

$$H_{CF} = B_2^0 O_2^0 + B_4^0 O_4^0 + B_4^3 O_4^3 + B_6^0 O_6^0 + B_6^3 O_6^3 + B_6^6 O_6^6. \quad (3)$$

Here, O_p^k are linear combinations of spherical tensor operators [53] (in the space of states with the fixed angular moment, operators O_p^k coincide with the Stevens operators). To fit the measured CF energies, the initial values of the CF parameters were estimated in the framework of the exchange-charge model (ECM) [54] (for details of the calculations see the Supplemental Material [43]).

The calculated CF parameters (see column 2 in Table IV) were used as the initial ones in the fitting of the measured CF levels of the Ho^{3+} ground and several excited multiplets. The fitting procedure based on the numerical diagonalization of the Hamiltonian H_0 [see Eq. (1)] in the total space of states of the $4f^{10}$ electronic configuration resulted in the set of CF parameters (see column 3 in Table IV) almost coinciding with the CF parameters obtained in Ref. [55] for the impurity Er^{3+} ions in LaAlO$_3$ (see column 4 in Table IV). The CF energies calculated making use of the final set of the CF parameters and

TABLE II. Measured and calculated CF energies (cm^{-1}) of the Ho^{3+} ions in LaAlO$_3$ and calculated g factors of the non-Kramers Γ_3 doublets.

$^{2S+1}L_J$		IR	Expt.	Theory	g Factor	$^{2S+1}L_J$		IR	Expt.	Theory	g Factor
$^5I_8$	A	Γ_1	0	0	0	$^5I_5$	A	Γ_3	11322.5	11319	0.144
	B	Γ_3	18	17.6	8.673		B	Γ_2	11332.5	11328	0
	C	Γ_3	133	136.4	2.509		C	Γ_3	11346.8	11344	2.106
	D	Γ_3	178	181.9	0.140		D	Γ_1	–	11346	0
	E	Γ_2	203	204.1	0		E	Γ_2	11387.1	11387	4.364
	F	Γ_1	249	257.8	0		F	Γ_3	11388.2	11385	0
	G	Γ_1	278	280.7	0		G	Γ_3	11416.5	11413	3.322
	H	Γ_3	288	298.0	11.068	$^5F_5$	A	Γ_3	15565	15576	8.901
	I	Γ_2	456	460.8	0		B	Γ_2	15610	15610	0
	J	Γ_3	471	475.8	6.320		C	Γ_3	15618	15618	5.076
	K	Γ_3	493	499.5	13.932		D	Γ_1	–	15627	0
$^5I_7$	A	Γ_2	5250.7	5252.9	0		E	Γ_3	15628	15627	3.482
	B	Γ_3	5260.6	5262.9	1.618		F	Γ_3	15662	15662	6.027
	C	Γ_3	5282.2	5283.6	2.604		G	Γ_2	15670	15670	0
	D	Γ_2	5290.5	5289.8	0	$^5S_2$	A	Γ_3	18571	18572	2.192
	E	Γ_1	5299.0	5296.1	0		B	Γ_1	–	18573	0
	F	Γ_3	5314.4	5314.5	7.164		C	Γ_3	18573	18574	0.648
	G	Γ_2	5323.3	5320.9	0	$^5F_4$	A	Γ_1	–	18575	0
	H	Γ_3	5325.4	5323.2	7.845		B	Γ_3	18661	18656	8.094
	I	Γ_1	5341.5	5340.2	0		C	Γ_2	18682	18679	0
	J	Γ_3	5360.4	5360.4	13.337		D	Γ_1	–	18683	0
$^5I_6$	A	Γ_2	8760.1	8755.7	0		E	Γ_3	18709	18700	0.713
	B	Γ_3	8765.2	8762.5	2.211		F	Γ_3	18787	18778	1.262
	C	Γ_1	8770.7	8767.4	0	$^5F_3$	A	Γ_1	–	20695	0
	D	Γ_3	8778.9	8777.2	2.654		B	Γ_3	20719	20717	0.78
	E	Γ_1	8803.0	8800.4	0		C	Γ_2	20756	20747	0
	F	Γ_2	8822.8	8820.5	0		D	Γ_3	20759	20752	2.79
	G	Γ_3	8829.2	8826.4	4.638		E	Γ_2	–	20830	0
	H	Γ_1	8847.0	8848.1	0						
	I	Γ_3	8870.0	8866.6	9.567						

presented in Table II agree satisfactorily with the experimental data. Table II contains also the calculated g factors, which determine splitting of the Γ_3 doublets in an external magnetic field directed along the c axis.

The obtained CF parameters are further used to calculate the hyperfine structure of the CF levels of Ho^{3+} in LaAlO$_3$. Holmium has only one stable isotope ^{165}Ho (100% abundant) with the nuclear spin $I = 7/2$. The total single-ion Hamiltonian operating in the space of electron-nuclear states can be written as follows:

$$H = H_0 + H_{\text{HFM}} + H_{\text{HFQ}} + H_{\text{el-def}}, \qquad (4)$$

where H_{HFM} and H_{HFQ} are the energies of magnetic and electric quadrupole hyperfine interactions, respectively, and $H_{\text{el-def}}$ is the Hamiltonian of the electron-deformation interaction.

The operators H_{HFM} and H_{HFQ} are presented in the Supplemental Material [43], and the operator $H_{\text{el-def}}$ linear in the crystal lattice deformations is considered in the next section, Sec. V. At the first step of the analysis of the observed line shapes, the electron-deformation interaction was neglected, and the energies of the electron-nuclear sublevels of the ^5I_J multiplets were computed by numerical diagonalization of the matrices of the operators H_{HFM} and H_{HFQ} constructed in the direct product of the subspace of electronic multiplet wave functions (i.e., the corresponding eigenfunctions of the Hamiltonian H_0) and the subspace of the nuclear states $|I = 7/2, I_z\rangle$.

In the first order of the perturbation theory, the magnetic hyperfine interaction does not change energies of electronic singlets Γ_1 and Γ_2, but splits the Γ_3 doublets into eight equidistant electron-nuclear doublet sublevels. However, the

TABLE III. Measured characteristics of the spectral lines corresponding to singlet-doublet transitions and the calculated hyperfine splitting of doublets. All values are in cm^{-1}.

Transition	Transition energy	Measured splitting	Half width	Hyperfine splitting (theory)
$\Gamma_1(^5I_8) \to \Gamma_3(^5I_7)$	5260.6	0.62	1.41	0.11
$\Gamma_1(^5I_8) \to \Gamma_3(^5I_7)$	5282.2	0.27	0.64	0.19
$\Gamma_1(^5I_8) \to \Gamma_3(^5I_6)$	8765.2	0.38	1.01	0.21
$\Gamma_1(^5I_8) \to \Gamma_3(^5I_6)$	8778.9	0.39	1.00	0.25
$\Gamma_1(^5I_8) \to \Gamma_3(^5I_5)$	11322.5	0.09	0.52	0.01

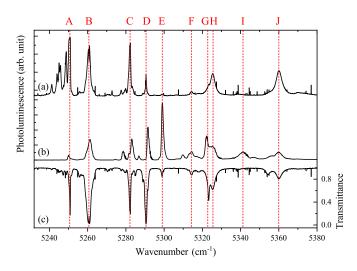FIG. 4. (a), (b) Luminescence spectra corresponding to the transitions from the lowest sublevel of the $^5S_2$ multiplet under (a) broadband excitation or (b) site-selective excitation (see text). (c) Transmission spectrum corresponding to the transitions between the ground state $\Gamma_1(^5I_8)$ and sublevels A–J of the excited multiplet $^5I_7$. $T = 5$ K. The intensity spectral distributions in (a), (b) are obtained by changing the sign of the frequency axis and the subsequent shift of the registered patterns to achieve the coincidence of the lines $A(^5S_2) \rightarrow A(^5I_7)$ with the line $A(^5I_8) \rightarrow A(^5I_7)$ in the transmission spectrum (c).

electric quadrupole hyperfine interaction and the mixing of the electronic CF states by the magnetic hyperfine interaction lead to additional shifts of the electron-nuclear sublevels and the nonequidistant hyperfine structures. The calculated total
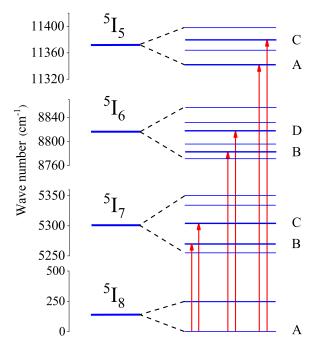

FIG. 5. Singlet-doublet transitions (arrows) with the resolved fine structure in the absorption spectra of Ho^{3+} ions in $LaAlO_3$ (thin and thick lines correspond to singlet and doublet CF levels, respectively).

hyperfine splittings of several singlet-doublet transitions are compared with the measurement data in Table III. The direct computations have shown that the contributions of the electric quadrupole hyperfine interaction into the hyperfine structure of the optical transitions can be neglected for most of the registered spectral lines. Figure 6, as well as Table III, show that the total width of the calculated hyperfine structures of the CF doublets is significantly smaller than the measured fine doublet structure of the corresponding spectral lines. This result clearly indicates the necessity to take into account the electron-deformation interaction.

V. ELECTRON-DEFORMATION INTERACTION

A. Parameters of the electron-deformation interaction

In the linear approximation, the interaction of $4f$ electrons with the crystal lattice deformations is defined by the operator

$$H_{\text{el-def}} = \sum_{\Gamma, \lambda} V(\Gamma, \lambda) e(\Gamma, \lambda), \qquad (5)$$

where $e(\Gamma, \lambda)$ are linear combinations of the deformation tensor components that transform according to the line λ of the IR Γ of the point symmetry group D_3:

$$e_1 = e(\Gamma_1^1) = (e_{xx} + e_{yy} + e_{zz})/\sqrt{6}, \ e_2$$
$$= e(\Gamma_1^2) = (2e_{zz} - e_{xx} - e_{yy})/\sqrt{12}, \qquad (6)$$

$$e_3 = e(\Gamma_3^1, 1) = (e_{xx} - e_{yy})/2, \quad e_4 = e(\Gamma_3^1, 2) = e_{xy}, \quad (7)$$

$$e_5 = e(\Gamma_3^2, 1) = e_{yz}, \quad e_6 = e(\Gamma_3^2, 2) = e_{xz}, \qquad (8)$$

and the electronic operators are written as follows:

$$V(\Gamma, \lambda) = \sum_{pk} b_p^k(\Gamma, \lambda) O_p^k. \qquad (9)$$

The parameters $b_p^k(\Gamma, \lambda)$ of the electron-deformation interaction (see Table S2 in the Supplemental Material [43]) were calculated in the framework of the exchange-charge model [54] using the same model parameters as in the calculations of the CF parameters. The fully symmetric $e(\Gamma_1^1)$ and $e(\Gamma_1^2)$ deformations shift all CF energy levels; the electronic Γ_3 doublets are split by the deformations $e(\Gamma_3^1, \lambda)$ and $e(\Gamma_3^2, \lambda)$. In real crystals, the deformation tensor is nonzero in the absence of external strains due to imperfection of the crystal lattice (various types of point defects, such as vacancies, interstitial or impurity ions, dislocations, and microscopic inhomogeneities). Components of the deformation tensor vary randomly at the positions of optical centers, and their observable characteristics should be averaged over the random fields of deformations.

B. Distribution function of random deformations

The distribution function of random deformations induced by point defects in LAO crystals was derived earlier in the
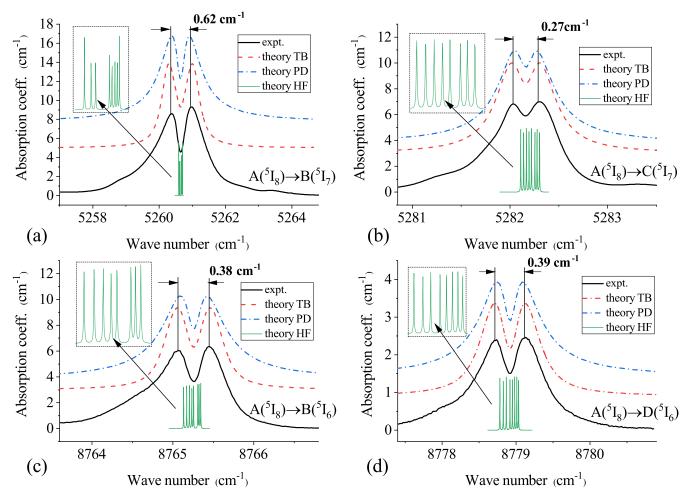
FIG. 6. Measured (solid lines) and calculated (dashed and dash-dotted lines) profiles of spectral lines corresponding to transitions between the ground singlet and the lowest doublets in the excited multiplets (a),(b) $^5I_7$ and (c),(d) $^5I_6$. The calculated hyperfine structure (HF) is shown in green in the lowest part of the figures and in the insets on enlarged scales. PD stands for point defects; TB stands for twin boundaries (see the text).

framework of the statistical theory in Ref. [35]:

$$g_{PD}(\boldsymbol{e}) = \frac{15\xi\nu_{\Gamma_1}}{8\pi^3\gamma_{\Gamma_1}^2\gamma_{\Gamma_3^1}^2\gamma_{\Gamma_3^2}^2}$$

$$\times\left(\frac{\nu_{\Gamma_1}^2\tilde{e}_1^2 + \tilde{e}_2^2}{\gamma_{\Gamma_1}^2} + \frac{e_3^2 + e_4^2}{\gamma_{\Gamma_3^1}^2} + \frac{e_5^2 + e_6^2}{\gamma_{\Gamma_3^2}^2} + \xi^2\right)^{-7/2}.$$

(10)

TABLE IV. CF parameters B_p^k (cm⁻¹) for the impurity Ho³⁺ and Er³⁺ ions in LaAlO₃

$p\ k$	Ho³⁺ calculated (ECM)	Ho³⁺ experimental	Er³⁺ [55]
1	2	3	4
2 0	−100.3	−159	−159
4 0	39.4	37.4	36.8
4 3	896.3	825.3	795.7
6 0	−56.8	−61.8	−61.8
6 3	645.3	762.1	762.1
6 6	−588.2	−585.2	−585.2

The dimensionless parameters $\nu_{\Gamma_1} = 5.88$, $\gamma_{\Gamma_1} = 26.2$, $\gamma_{\Gamma_3^1} = 30.7$, and $\gamma_{\Gamma_3^2} = 31.2$ were found using the elastic constants of LaAlO₃ in the rhombohedral phase. The sample-dependent parameter $\xi = |\Omega|C_d/48\pi$ is linear in the concentration C_d of point defects and the defect strength Ω. The latter can be considered as the change of a unit cell volume induced by a single defect [36]. Note that the products $\xi\gamma_\Gamma$ and $\xi(\gamma_\Gamma/\nu_\Gamma)$ determine widths of distributions for deformations $e(\Gamma)$. The components of the deformation tensor, marked with a tilde, are linear combinations of the symmetrized components introduced above, transforming according to the same IR Γ_1:

$$\tilde{e}_1 = e_1\cos\psi + e_2\sin\psi, \quad \tilde{e}_2 = -e_1\sin\psi + e_2\cos\psi,$$

(11)

where $\psi = 7.4°$ [35]. The value of the parameter ξ can be determined from a comparison of the measured and simulated envelopes and deformation splittings of the spectral lines.

Deformations of the crystal lattice of LAO (compression along one of the four C_3 axes) induce four possible twin-domain states [32]. There are three rhombohedral twin boundary arrangements in accordance with possible planes of contact: pure {100} or {110}, and mixed {100}/{110} [56].

Let us consider two domains with deformations along two different C_3 axes contacting through the {100} plane, i.e., the face of the parent cubic cell. We can write for each domain the deformation tensors $e_{\alpha\beta}$ which transform the crystal from the cubic into the rhombohedral phase in the following form (in cubic axes) [32]:

$$\boldsymbol{e}_{\text{I}} = \begin{pmatrix} 0 & \bar{\varepsilon} & \bar{\varepsilon} \\ \bar{\varepsilon} & 0 & \bar{\varepsilon} \\ \bar{\varepsilon} & \bar{\varepsilon} & 0 \end{pmatrix}, \quad \boldsymbol{e}_{\text{II}} = \begin{pmatrix} 0 & \varepsilon & \bar{\varepsilon} \\ \varepsilon & 0 & \varepsilon \\ \bar{\varepsilon} & \varepsilon & 0 \end{pmatrix}. \quad (12)$$

The deformation at the twin-domain boundary can be introduced as follows: $\boldsymbol{e}^{\text{TB}} = (\boldsymbol{e}_{\text{I}} + \boldsymbol{e}_{\text{II}})/2$. This definition results in a single nonzero component $e_{13}^{\text{TB}} = e_{31}^{\text{TB}} \equiv \varepsilon$ of the deformation tensor. We suppose that these deformations also contribute into the observed deformation splittings of spectral lines, just like the point defects. In the calculations of the shifts and splittings of the CF energy levels caused by the interaction of the Ho^{3+} ions with deformations induced by the twin-domain boundaries, the deformation tensor components in the Hamiltonian (5), defined in the local Cartesian system of coordinates with the z axis along the C_3 symmetry axis, were expressed through the deformation ε introduced in the global cubic crystallographic axes.

The distribution function of random deformations induced by the domain walls is approximated by the Lorentz distribution (we assume alternating signs of deformations between adjacent walls):

$$g_{\text{TB}}(\varepsilon) = \frac{\gamma_{\text{TB}}}{\pi} \big[(\varepsilon - \langle \varepsilon \rangle)^2 + \gamma_{\text{TB}}^2 \big]^{-1}, \quad (13)$$

where $\langle \varepsilon \rangle$ is the average value of the deformation ε in a domain and γ_{TB} is the distribution width determined by comparing the simulation results with the measured spectral line profiles.

VI. LINE SHAPE OF SINGLET-DOUBLET TRANSITIONS

We simulated the observed profiles of spectral lines corresponding to singlet-doublet transitions, assuming broadening and the formation of a fine doublet structure due to the interaction of the Ho^{3+} ions with random deformations of the crystal lattice induced by point defects and twin-domain boundaries.

The envelope of the singlet-doublet transition in the absorption (luminescence) spectrum is calculated by averaging the form functions $I_0(x)$ of individual magnetic- or electric-dipole transitions between the hyperfine sublevels of a CF singlet and a CF doublet in the field of fixed deformations $\boldsymbol{e}$ over the distribution function of random deformations:

$$I(\omega) = \int g(\boldsymbol{e}) \sum_{m=\frac{1}{2}, \frac{3}{2}, \frac{5}{2}, \frac{7}{2}} (I_0[\hbar(\omega - \omega_0) - \varepsilon_m^{(+)}(\boldsymbol{e})]$$

$$+ I_0[\hbar(\omega - \omega_0) - \varepsilon_m^{(-)}(\boldsymbol{e})]) d\boldsymbol{e}. \quad (14)$$

Here ω_0 is the frequency of a transition between CF levels in the absence of lattice deformations and

$$\varepsilon_m^{(\pm)}(\boldsymbol{e}) = \eta_1 e_1 + \eta_2 e_2 \pm \big[(Am)^2 + \eta_3^2 (e_3 + e_4) + \eta_5^2 (e_5 + e_6) \big.$$

$$\big. + 2\eta_3\eta_5 (e_3 e_5 - e_4 e_6) \big]^{1/2}. \quad (15)$$

$\varepsilon_m^{(\pm)}(\boldsymbol{e})$ are shifts of hyperfine sublevels of the CF doublet induced by deformations and the magnetic hyperfine interaction (we neglect here the quasiquadrupole effects). The constants of coupling with deformations η_1, η_2 and η_3, η_5 equal to matrix elements $\langle \Gamma_3, 1 | V(\Gamma_1^1) | \Gamma_3, 1 \rangle$, $\langle \Gamma_3, 1 | V(\Gamma_1^2) | \Gamma_3, 1 \rangle$ and $\langle \Gamma_3, 1 | V(\Gamma_3^1, 1) | \Gamma_3, 2 \rangle$, $\langle \Gamma_3, 1 | V(\Gamma_3^2, 1) | \Gamma_3, 2 \rangle$, respectively, where operators $V(\Gamma, \lambda)$ are defined by Eq. (9), and $| \Gamma_3, \alpha \rangle$ ($\alpha = 1, 2$) are the wave functions of the corresponding doublet, built as the eigenfunctions of the electronic magnetic moment operator projected on the C_3 axis. The calculated values of the coupling constants η_1, η_2, η_3, and η_5 for doublets with the resolved deformation splitting are presented in Table S3 in the Supplemental Material [43]. The hyperfine structure interval A equals $|\langle \Gamma_3, 1 | a_z | \Gamma_3, 1 \rangle|$, where the operator a_z is the z component of the vector operator $\boldsymbol{a}$ in the energy of the magnetic hyperfine interaction $H_{\text{HFM}} = \boldsymbol{aI}$ (see Eq. (S4) in the Supplemental Material [43]). The form function of individual transitions is approximated by the Lorentz distribution $I_0(x) = (2\pi\Delta^2)^{-1/2} \exp(-x^2/2\Delta^2)$ with the half width $\Delta = 0.078$ cm^{-1}.

From the fitting of the measured line profiles by varying the parameter ξ in the distribution function (10) for deformations induced by point defects, the best results were obtained using the value of $\xi = 2.7 \times 10^{-5}$. Both types of point defects, i.e., Ho^{3+} impurity ions as well as intrinsic lattice defects (IDs), contribute to this value. Assuming the additivity of these contributions, we obtain the relation

$$\xi = \xi_{\text{Ho}} + \xi_{\text{ID}} = \frac{(C_{\text{Ho}} |\Omega_{\text{Ho}}| + C_{\text{ID}} |\Omega_{\text{ID}}|)}{48\pi}, \quad (16)$$

which allows us to estimate the relative role of intrinsic lattice defects. In particular, the defect strength for impurity Tm^{3+} ions substituting for Lu^{3+} ions in the oxygen surroundings in $LuPO_4$ crystals has been determined in Ref. [37], $\Omega_{\text{Tm}} \sim 1$ Å^3. Supposing the linear dependence of the defect strength on the difference between volumes of the impurity and the substituted lattice ions, we obtained the defect strength $\Omega_{\text{Ho}} = \Omega_{\text{Tm}} (V_{\text{Ho}^{3+}} - V_{\text{La}^{3+}}) / (V_{\text{Tm}^{3+}} - V_{\text{Lu}^{3+}}) = -8.5$ Å^3 for Ho^{3+} ions in LAO by making use of corresponding ionic radii from Ref. [38]. The volume concentration $C_{\text{Ho}} = 1.2 \times 10^{-4}$ Å^{-3} of Ho^{3+} ions was estimated using the nominal weight concentration. Thus, we obtained the contribution of the impurity ions into the width of the distribution function of random deformations $\xi_{\text{Ho}} = 0.7 \times 10^{-5}$. A comparison of this value with the total experimental width $\xi = 2.7 \times 10^{-5}$ shows that intrinsic defects play the dominant role in the deformation broadening and splittings of spectral lines in the studied sample of $LaAlO_3$:Ho.

The distribution function of random deformations given by Eq. (13) was used to account for the strains induced by boundaries of the ferroelastic domains. As a result of the fitting of measured profiles of spectral lines, we obtained the mean value of deformations $\langle \varepsilon \rangle = \pm 5 \times 10^{-4}$ and the distribution widths γ_{TB} for different singlet-doublet transitions in the range $(3–6) \times 10^{-4}$. In absolute values, $\langle \varepsilon \rangle$ is substantially smaller than the spontaneous strain tensor component $e_4 = -22 \times 10^{-4}$ in the rhombohedral phase of LAO at low temperatures [30].

The two theoretical envelopes of spectral lines in Figs. 6(a)–6(d) represent the results of modeling in the

frameworks of the approaches based on the averaging procedures with two different distribution functions for random deformations induced by point defects and the twin-domain boundaries. Both approaches allow us to successfully reproduce deformation splittings (differences of the energies corresponding to maxima in the profiles of singlet-doublet transitions) and the total linewidths. The shapes of the spectral envelopes differ only at the wings of the fine doublet structure; namely, the envelopes obtained within the point-defect approach have a more smooth decay and agree better with the measured line shapes. For more precise estimations of mean deformations of different symmetry, more elaborated theory of deformations induced by domain walls and additional studies of LAO crystals with different concentrations of impurity ions are necessary.

VII. CONCLUSION

We measured high-resolution absorption and luminescence as well as site-selective laser excitation and emission spectra of the LaAlO$_3$ crystal doped with the Ho^{3+} ions in a wide range of wavelengths at low temperatures. The analysis of the high-resolution spectra and of the results of selective laser spectroscopy allowed us to determine the energies of the CF levels of the ground and excited ^5I_J ($J = 5$–8), $^5F_5$, $^5S_2$, $^5F_4$ multiplets of the Ho^{3+} ion. The CF parameters are calculated taking into account the displacements of the ions located in the nearest environment of the optical center. The results of calculating the CF structure of the energy spectrum of the holmium ion in the LaAlO$_3$ crystal are in good agreement with the measured data.

In the optical spectra, the lines of singlet-doublet transitions of holmium ions with a specific doublet structure were registered. The parameters of the electron-deformation interaction in the LaAlO$_3$ crystal, calculated within the framework of the exchange-charge model, were used to simulate the shape of the spectral lines. In particular, within the framework of the model of deformation broadening and splitting of spectral lines caused by random strains of the crystal lattice, the envelopes of lines corresponding to transitions from the ground orbital singlet [$^5I_8$ (Γ_1)] to doublets Γ_3 of excited multiplets ($^5I_{7,6,5}$) were calculated. Two mechanisms of the formation of deformations are considered, namely, deformations caused by (i) point defects and (ii) stresses at the boundaries of contacting ferroelectric domains. The Lorentzian distribution function of random strains induced by domain boundaries is introduced. The parameters of the distribution function were obtained from a comparison of the simulation results and the envelopes of spectral lines observed in the optical spectrum.

The deformation broadening model made it possible to estimate the contribution from *intrinsic* defects to the width of the distribution function of deformations induced by lattice defects. The calculation showed that this contribution can be 75%. This indicates the presence of other than impurity ion sources of the crystal-structure distortion in the LaAlO$_3$ crystal, which can be oxygen vacancies and boundaries of ferroelastic domains.

The results of our research can be applied to quantitatively estimate the quality of crystals and the contribution of various types of defects to random lattice deformations. Such estimates are helpful when choosing optimal materials for heterogeneous structures in ferroelectric devices, in particular, containing LaAlO$_3$ layers, in modern technologies, e.g., quantum information processing and quantum electronics.

[1] W. Li and L.-J. Ji, Perovskite ferroelectrics go metal free, Science **361**, 132 (2018).

[2] T. Zheng, J. Wu, D. Xiao, and J. Zhu, Recent development in lead-free perovskite piezoelectric bulk materials, Prog. Mater. Sci. **98**, 552 (2018).

[3] W. Eerenstein, N. D. Mathur, and J. F. Scott, Multiferroic and magnetoelectric materials, Nature **442**, 759 (2006).

[4] E. Dagotto, T. Hotta, and A. Moreo, Colossal magnetoresistant materials: The key role of phase separation, Phys. Rep. **344**, 1 (2001).

[5] C. N. R. Rao, Perovskite oxides and high-temperature superconductivity, Ferroelectrics **102**, 297 (1990).

[6] M. A. Green, A. Ho-Baillie, and H. J. Snaith, The emergence of perovskite solar cells, Nat. Photonics **8**, 506 (2014).

[7] A. K. Jena, A. Kulkarni, and T. Miyasaka, Halide perovskite photovoltaics: Background, status, and future prospects, Chem. Rev. **119**, 3036 (2019).

[8] Z. Wei and J. Xing, The rise of perovskite light-emitting diodes, J. Phys. Chem. Lett. **10**, 3035 (2019).

[9] Q. Zhang, H. Sun, H. Zhang, M. Jiang, X. Wu, Zh. Zhang, T. Yang, R. Xia, and J. Cabanillas-Gonzalez, Facile and controllable fabrication of high-performance methylammonium lead triiodide films using lead acetate precursor for low-threshold amplified spontaneous emission and distributed-feedback lasers, Phys. Status Solidi RRL **13**, 1900176 (2019).

[10] Y. Wang, L. Song, Y. Chen, and W. Huang, Emerging new-generation photodetectors based on low-dimensional halide perovskites, ACS Photonics **7**, 10 (2020).

[11] M. A. Haque, S. Kee, D. R. Villalva, W.-L. Ong, and D. Baran, Halide perovskites: Thermal transport and prospects for thermoelectricity, Adv. Sci. **7**, 1903389 (2020).

[12] J. Xu, D. Murata, B. So, K. Asami, J. Ueda, J. Heo, and S. Tanabe, 1.2 μm persistent luminescence of Ho^{3+} in LaAlO$_3$ and LaGaO$_3$ perovskites, J. Mater. Chem. C **6**, 11374 (2018).

[13] J. Zylberberg and Z.-G. Ye, Improved dielectric properties of bismuth-doped LaAlO₃, J. Appl. Phys. **100**, 086102 (2006).

[14] S-G. Lim, S. Kriventsov, T. N. Jackson, J. H. Haeni, D. G. Schlom, A. M. Balbashov, R. Uecker, P. Reiche, J. L. Freeouf, and G. Lucovsky, Dielectric functions and optical bandgaps of high-*K* dielectrics for metal-oxide-semiconductor field-effect transistors by far ultraviolet spectroscopic ellipsometry, J. Appl. Phys. **91**, 4500 (2002).

[15] X. B. Lu, H. B. Lu, Z. H. Chen, X. Zhang, R. Huang, H. W. Zhou, X. P. Wang, B. Y. Nguyen, C. Z. Wang, W. F. Xiang, M. He, and B. L. Cheng, Field-effect transistors with LaAlO₃ and LaAlO$_x$N$_y$ gate dielectrics deposited by laser molecular-beam epitaxy, Appl. Phys. Lett. **85**, 3543 (2004).

[16] M. Esro, R. Mazzocco, G. Vourlias, O. Kolosov, A. Kreir, and W. I. Milne, Solution processed lanthanum aluminate gate dielectrics for use in metal oxide-based thin film transistors, Appl. Phys. Lett. **106**, 203507 (2015).

[17] R. Spinicci, P. Marini, S. De Rossi, M. Faticanti, and P. Porta, Oxidative coupling of methane on LaAlO₃ perovskites partially substituted with alkali or alkali-earth ions, J. Mol. Catal. A: Chem. **176**, 253 (2001).

[18] P. Venkataswamy, M. Sudheera, K. Vaishnavi, K. Ramaswamy, G. Ravi, and M. Vithal, A new Ag/AgBr/LaAlO₃ plasmonic composite: Synthesis, characterization, and visible-light driven photocatalytic activity, J. Electron. Mater. **49**, 2358 (2020).

[19] A. Ohtomo and H. Y. Hwang, A high-mobility electron gas at the LaAlO₃/SrTiO₃ heterointerface, Nature **427**, 423 (2004).

[20] L. Chen, E. Sutton, H. Lee, J.-W. Lee, J. Li, Ch.-B. Eom, P. Irvin, and J. Levy, Over 100-THz bandwidth selective difference frequency generation at LaAlO₃/SrTiO₃ nanojunctions, Light: Sci. Appl. **8**, 24 (2019).

[21] P. J. Deren, Spectroscopic characterization of LaAlO₃ crystal doped with Pr³⁺ ions, J. Lumiun. **122-123**, 40 (2007).

[22] P. J. Deren and J.-C. Krupa, Spectroscopic investigations of LaAlO₃:Eu³⁺, J. Lumin. **102-103**, 386 (2003).

[23] P. J. Deren and J.-C. Krupa, Spectroscopic properties of LaAlO₃ crystal doped with Ho³⁺, J. Alloys Compds. **380**, 362 (2004).

[24] P. J. Deren and R. Mahiou, Spectroscopic characterization of LaAlO₃ crystal doped with Er³⁺ ions, Opt. Mater. **29**, 766 (2007).

[25] A. Gocalinska, P. J. Deren, P. Gluchowski, Ph. Goldner, and O. Guiollot-Noël, Spectroscopic characterization of LaAlO₃ crystal doped with Tm³⁺ ions, Opt. Mater. **30**, 680 (2008).

[26] P. J. Deren, R. Mahiou, and Ph. Goldner, Multiphonon transitions in LaAlO₃ doped with rare earth ions, Opt. Mater. **31**, 465 (2009).

[27] P. J. Deren, K. Lemański, A. Gągor, A. Watras, M. Małecka, and M. Zawadzki, Symmetry of LaAlO₃ nanocrystals as a function of crystallite size, J. Solid State Chem. **183**, 2095 (2010).

[28] M. Mączka, E. Mendoza-Mendoza, A. F. Fuentes, and K. Lemański, Low-temperature synthesis, luminescence, and phonon properties of Er and/or Dy doped LaAlO₃ nanopowders, J. Solid State Chem. **187**, 249 (2012).

[29] P. J. Deren, A. Bednarkiewicz, Ph. Goldner, and O. Guillot-Noël, Laser action in LaAlO₃:Nd³⁺ single crystal, J. Appl. Phys. **103**, 043102 (2008).

[30] S. A. Hayward, F. D. Morrison, S. A. T. Redfern, E. K. H. Salje, J. F. Scott, K. C. Knight, S. Tarantino, A. M. Glazer, V. Shuvaeva, P. Daniel, M. Zhang, and M. A. Carpenter, Transformation processes in LaAlO₃: Neutron diffraction, dielectric,

[31] M. Karbowiak, P. Gnutek, and C. Rudowicz, Crystal-field analysis for RE³⁺ ions in laser materials: III. Energy levels for Nd³⁺ and Er³⁺ ions in LaAlO₃, YAlO₃, and LaGaO₃ single crystals—combined approach to low symmetry crystal field parameters, Chem. Phys. **400**, 29 (2012).

[32] S. Bueble, K. Knorr, E. Brecht, and W. W. Schmahl, Influence of the ferroelastic twin domain structure on the {100} surface morphology of LaAlO₃/HTSC substrates, Surf. Sci. **400**, 345 (1998).

[33] N. Pelletier-Allard and F. Martin-Brunetière, Étude théorique des spectres optiques des ions Pr³⁺ dans AlLaO₃, J. Phys. (Paris) **30**, 849 (1969).

[34] S. A. Klimin, D. S. Pytalev, M. N. Popova, B. Z. Malkin, M. V. Vanyunin, and S. L. Korableva, High-resolution optical spectroscopy of Tm³⁺ ions in LiYF₄: Crystal-field energies, hyperfine and deformation splittings, and the isotopic structure, Phys. Rev. B **81**, 045113 (2010).

[35] N. M. Abishev, E. I. Baibekov, B. Z. Malkin, M. N. Popova, D. S. Pytalev, and S. A. Klimin, Deformation broadening and the fine structure of spectral lines in optical spectra of dielectric crystals containing rare-earth ions, Phys. Solid State **61**, 795 (2019).

[36] B. Z. Malkin, D. S. Pytalev, M. N. Popova, E. I. Baibekov, M. L. Falin, K. I. Gerasimov, and N. M. Khaidukov, Random lattice deformations in rare earth doped cubic hexafluoroelpasolites: High-resolution optical spectroscopy and theoretical studies, Phys. Rev. B **86**, 134110 (2012).

[37] B. Z. Malkin, N. M. Abishev, E. I. Baibekov, D. S. Pytalev, K.N. Boldyrev, M. N. Popova, and M. Bettinelli, Distribution function of random strains in elastically anisotropic continuum and defect strengths of impurity Tm³⁺ ions in crystals with zircon structure, Phys. Rev. B **96**, 014116 (2017).

[38] R. D. Shannon, Revised effective ionic radii and systematic studies of interatomic distances in halides and chalcogenides, Acta Crystallogr., Sect. A **32**, 751 (1976).

[39] O. A. Dicks, A. L. Shluger, P. V. Sushko, and P. B. Littlewood, Spectroscopic properties of oxygen vacancies in LaAlO₃, Phys. Rev. B **93**, 134114 (2016).

[40] M. Choi, A. Janotti, and C. G. Van de Walle, Native point defects in LaAlO₃: A hybrid functional study, Phys. Rev. B **88**, 214117 (2013).

[41] W. T. Carnall, G. L. Goodman, K. Rajnak, and R. S. Rana, A systematic analysis of the spectra of the lanthanides doped into single crystal LaF₃, J. Chem. Phys. **90**, 3443 (1989).

[42] A. Baraldi, R. Capelletti, M. Mazzera, N. Magnani, I. Földvári, and E. Beregi, Hyperfine interaction in YAB:Ho³⁺: A high-resolution spectroscopy investigation, Phys. Rev. B **76**, 165130 (2007).

[43] See Supplemental Material at http://link.aps.org/supplemental/10.1103/PhysRevB.103.054103 for the parameters of the free-ion Hamiltonian (2), the details of calculations of the CF parameters, and the parameters of the electron-deformation interaction; also see [44–52].

[44] R. M. Sternheimer, M. Blume, and R. F. Peierls, Shielding of crystal fields at rare-earth ions, Phys. Rev. **173**, 376 (1968).

[45] O. J. Sovers, Trivalent lanthanide 4 *f* electron radial wave functions, J. Phys. Chem. Solids **28**, 1073 (1967).

[46] E. Clementi and A. D. McLean, Atomic negative ions, Phys. Rev. **133**, A419 (1964).

[47] C. Howard, B. J. Kennedy, and B. C. Chakoumakos. Neutron powder diffraction study of rhombohedral rare-earth aluminates and the rhombohedral to cubic phase transition, J. Phys.: Condens. Matter **12**, 349 (2000).

[48] A. Abragam and B. Bleaney, *Electron Paramagnetic Resonance of Transition Ions* (Clarendon Press, Oxford, 1970).

[49] D. S. Pytalev, E. P. Chukalina, M. N. Popova, G. S. Shakurov, S. L. Korableva, and B. Z. Malkin, Hyperfine interactions of Ho^{3+} ions in KY$_3$F$_{10}$: Electron paramagnetic resonance and optical spectroscopy studies, Phys. Rev. B **86**, 115124 (2012).

[50] M. A. H. McCausland and I. S. Mackenzie, Nuclear magnetic resonance in rare earth metals, Adv. Phys. **28**, 305 (1979).

[51] R. P. Gupta and S. K. Sen, Sternheimer shielding-antishielding; Rare-earth ions, Phys. Rev. A **7**, 850 (1973).

[52] P. Raghavan, Table of nuclear moments, At. Data Nucl. Data Tables **42**, 189 (1989).

[53] V. V. Klekovkina, A. R. Zakirov, B. Z. Malkin, and L. A. Kasatkina. Simulations of magnetic and magnetoelastic properties of Tb$_2$Ti$_2$O$_7$ in paramagnetic phase, J. Phys.: Conf. Ser. **324**, 012036 (2011).

[54] B. Z. Malkin, Crystal field and electron-phonon interaction in rare-earth ionic paramagnet, in *Spectroscopy of Solids Containing Rare-Earth Ions*, edited by A. A. Kaplyanskii and R. M. Macfarlane (Elsevier Science Publishers, Amsterdam, 1987). Chap. 2, pp. 13–49.

[55] E. Antic-Fidancev, P. J. Deren, and J.-C. Krupa, Energy levels and crystal field calculations of Er^{3+} in LaAlO$_3$, J. Alloys Compds. **380**, 376 (2004).

[56] P. A. Vermeulen, A. Kumar, G. H. ten Brink, G. R. Blake, and B. J. Kooi, Unravelling the domain structures in GeTe and LaAlO$_3$, Crystal Growth Des. **16**, 5915 (2016).